Microchemical Journal 218 (2025) 115600

Contents lists available at ScienceDirect

Microchemical Journal

journal homepage: www.elsevier.com/locate/microc

CuO-modified graphitic carbon nitride as a bifunctional platform for organic pollutant reduction and plasmonic detection of cadmium ions

Muradiye Şahin [a,b,*,1]

[a] Department of Chemistry, Selcuk University, Campus, 42075 Konya, Turkey
[b] Kırşehir Ahi Evran University, Campus, 40100 Kırşehir, Turkey

ARTICLE INFO

Keywords:
Methyl orange
Acetamiprid
Graphitic carbon nitride
Heterogeneous catalyst
Plasmonic sensor

ABSTRACT

In this study, the facile two-step synthesis of CuO-modified graphitic carbon nitride (CuO@g-C_3N_4) hybrid nanosheets with catalytic and sensing functions was carried out. Pristine g-C_3N_4, obtained by thermal polymerization of melamine, was surface-engineered with in-situ deposited CuO nanoparticles, resulting in a uniform nanocomposite with abundant active sites and enhanced electron-transfer capability. Structural (XRD), optical (UV–Vis), and morphological (SEM-EDS, TEM) characterizations confirmed the successful formation of a p–n heterojunction, a narrowed bandgap (from 2.55 eV to 1.84 eV), and a uniform distribution of CuO nanoparticles across the g-C_3N_4 layers. The hybrid material exhibited excellent catalytic activity for the $NaBH_4$-assisted degradation of methyl orange (MO) and acetamiprid (ACT), achieving rapid pollutant removal as described by pseudo-first-order kinetics. Furthermore, CuO@g-C_3N_4 demonstrated a pronounced bathochromic surface plasmon resonance (SPR) shift upon Cd^{2+} ion interaction, enabling its application as a plasmonic fluorescence sensor. Detection parameters revealed limits of detection (LOD) and quantification (LOQ) of 107.6 μM and 358.7 μM, respectively. While g-C_3N_4-based composites combining photocatalysis with sensing have been previously reported, to the best of our knowledge this is the first demonstration on a CuO@g-C_3N_4 platform that integrates $NaBH_4$-assisted catalytic reduction of an azo dye and a neonicotinoid pesticide in the dark with Cd^{2+} detection via an SPR-mediated fluorescence response, providing a cost-effective route for environmental remediation and monitoring.

1. Introduction

Water is an indispensable resource for all forms of life, yet its quality is increasingly threatened each year by pollutants such as pharmaceuticals, textile dyes, and pesticides [1]. Dyes released from textile industries pose significant ecological hazards due to their carcinogenic, mutagenic, and ecotoxic nature [2,3]. Methyl orange (MO), an azo dye, has been reported to cause severe health effects, including pulmonary tissue degeneration, cardiac palpitations, and vomiting [4]. Acetamiprid (ACT), a neonicotinoid insecticide, is widely employed in agriculture owing to its high insecticidal efficiency and selectivity [5]. However, its high water solubility (4.25 g/L) [6] and soil mobility [7–9] lead to persistent micro-pollution in aquatic environments. Human exposure to ACT has been associated with neurodevelopmental disorders, congenital heart defects, memory loss, and tremors [10–13], while its environmental persistence also threatens aquatic organisms, soil microbiota, and beneficial insects [14–16]. These concerns necessitate the development of effective strategies for the removal of ACT and MO from contaminated water bodies [17]. Various methods have been explored for the removal and/or degradation of these pollutants, including oxidation [18,19], photocatalysis [20,21], coagulation [22], liquid–liquid extraction [23], ozonation [24], adsorption [25–28], aerobic degradation [29,30], and nanofiltration [31–34]. Among these, heterogeneous chemical catalysis has emerged as a promising alternative due to its environmental friendliness, high efficiency, operational simplicity, and ability to proceed under mild reaction conditions [35]. This approach enables the rapid degradation of toxic chemicals using reducing agents such as sodium borohydride ($NaBH_4$), and it is economically favorable compared to photocatalysis, as it does not require expensive light sources or large band gaps for photoactivation [36].

Graphitic carbon nitride (g-C_3N_4) is a metal-free, two-dimensional

* Corresponding author at: Department of Chemistry, Selcuk University, Campus, 42075 Konya, Turkey.
E-mail address: muradiye.sahin@ahievran.edu.tr.
[1] ORCID ID:0000–0002–5445-6682.

https://doi.org/10.1016/j.microc.2025.115600
Received 14 August 2025; Received in revised form 8 September 2025; Accepted 30 September 2025
Available online 1 October 2025
0026-265X/© 2025 Elsevier B.V. All rights are reserved, including those for text and data mining, AI training, and similar technologies.

polymeric semiconductor composed of tri-*s*-triazine units linked through amino bridges, with adjacent layers held together by van der Waals forces [37,38]. Owing to its moderate band gap, high mechanical strength, low cost, and exceptional chemical and thermal stability, g-C_3N_4 has attracted attention in diverse applications, including sorption, catalysis, nanofillers, sensing, and optoelectronics [37–39]. Its facile synthesis from abundant nitrogen-rich precursors such as urea and melamine, coupled with its non-toxicity, makes it an appealing candidate for heterogeneous catalysis [40]. g-C_3N_4-based catalysts have been successfully applied in bacterial inactivation [41], CO_2 reduction [42], degradation of chemical pollutants [43], water splitting [44] and sensor development [45]. One effective strategy to enhance the conductivity and redox efficiency of g-C_3N_4 is to couple it with narrow-band-gap semiconductors [46–48]. Copper(II) oxide (CuO) nanoparticles are especially attractive due to their natural abundance, low cost, high catalytic activity, narrow band gap, and suitability for large-scale applications [49]. When incorporated into g-C_3N_4, CuO can not only improve charge separation and electron transport but also provide additional active sites, thereby enhancing both catalytic and sensing performances.

In this work, CuO@g-C_3N_4 hybrid nanosheets were synthesized through a facile two-step calcination method. In the first step, g-C_3N_4 was obtained via thermal condensation of melamine, followed by immobilization of CuO nanoparticles in the second step. The resulting materials were comprehensively characterized and systematically tested for the $NaBH_4$-assisted reduction of MO and ACT under varying catalyst and reductant concentrations. Moreover, the potential of CuO@g-C_3N_4 as a plasmonic sensor for Cd^{2+} detection in the 200–800 μM concentration range was investigated. To the best of my knowledge, this study is the first to report the dual functionality of CuO@g-C_3N_4 for both the reduction of an azo dye and a neonicotinoid pesticide, alongside its selective plasmonic detection of Cd^{2+} ions, thereby providing a cost-effective and multifunctional platform for environmental remediation.

2. Materials and methods

2.1. CuO@g-C_3N_4 hybrid nanocatalyst preparation

g-C_3N_4 was synthesized via a thermal exfoliation method. Briefly, 5 g of melamine powder ($C_3H_6N_6$, 99 %, Sigma-Aldrich) was placed in a covered alumina crucible and heated at 550 °C for 4 h at a ramp rate of 10 °C min^{-1} [50]. The resulting yellow porous nanosheets of g-C_3N_4 were collected after cooling to room temperature.

The CuO@g-C_3N_4 hybrid was synthesized following the procedure of Atacan and Özacar with slight modifications [51]. In a typical process, 0.012 g of g-C_3N_4 was dispersed in 20 mL of deionized water (18.2 MΩ·cm, Millipore Milli-Q Plus) via ultrasonication for 3 h. Separately, 0.60 g of copper(II) nitrate trihydrate ($Cu(NO_3)_2{\cdot}3H_2O$, 99 %, Merck) was dissolved in deionized water, followed by the dropwise addition of 2 mL of 0.5 M NaOH (97 %, Merck) under stirring. The g-C_3N_4 dispersion was then added to this mixture and stirred magnetically for 30 min. The mixture was transferred to a Teflon-lined stainless steel autoclave and subjected to hydrothermal treatment at 180 °C for 16 h. The product was washed three times with ethanol (99.2 %, Merck) and deionized water, then dried at 70 °C for 15 h. A schematic illustration of the synthesis procedure and the structure of the hybrid nanolayer is presented in Scheme 1. To optimize catalytic performance, CuO@g-C_3N_4 was prepared at different mass ratios of CuO:g-C_3N_4 (100:1, 50:1, and 10:1, *w/w*). The composite with the highest catalytic activity (50:1 ratio) was selected for all subsequent experiments. This optimization ensured a balance between sufficient CuO loading for catalytic activity and the preservation of g-C_3N_4's intrinsic surface area and structural integrity.

2.2. CuO@g-C_3N_4 hybrid nanocatalyst characterization techniques

The morphology of the synthesized materials was examined using a scanning electron microscope (SEM; Jeol JSM-IT300) coupled with an energy-dispersive X-ray spectroscopy (EDS; Bruker XFlash 6130) for elemental mapping and composition analysis. The crystalline structures were investigated via X-ray diffraction (XRD; Bruker D8 Advance) using

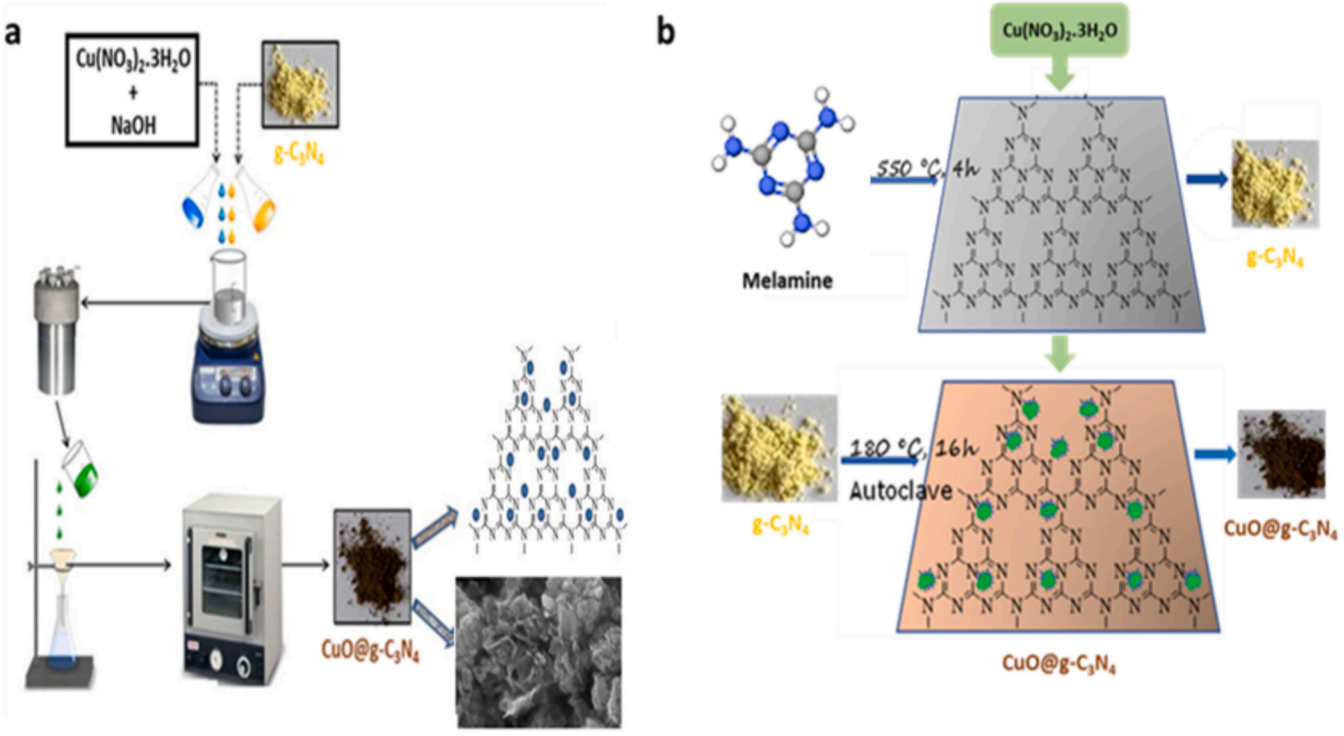

Scheme 1. Illustration of (a) the synthesis procedure and (b) schematic route for the preparation of CuO-decorated g-C_3N_4 hybrid catalyst

Cu Kα radiation (λ = 1.5406 Å) at 40 kV, scanning from 10° to 80° (2θ) with a step size of 0.02°. Optical properties were analyzed using UV–visible spectroscopy (UV–vis; Shimadzu UV-3600) in the range of 200–800 nm with $BaSO_4$ as the reference. The optical band gap energies were calculated using the Kubelka–Munk function. Fourier-transform infrared (FT-IR) spectra were recorded using a Bruker FT-IR spectrometer in the range of 400–4000 cm^{-1} to identify functional groups and confirm chemical bonding. The HRTEM depictions were caught spending a JEOL JEM-2100 Transmission Electron Microscope (TEM). This combination of structural, morphological, and optical analyses allowed for a comprehensive understanding of the relationship between the hybrid's physicochemical properties and its catalytic/sensing performance.

2.3. Evaluation of catalytic activity for MO and ACT degradation

The catalytic activity of CuO@g-C_3N_4 was assessed by monitoring the $NaBH_4$-assisted reduction of methyl orange (MO; $C_{14}H_{14}N_3NaO_3S$, Merck) and acetamiprid (ACT; $C_{10}D_3H_8ClN_4$, Sigma-Aldrich). Stock solutions were prepared by dissolving the respective compounds in deionized water. Degradation reactions were performed at room temperature. The reaction mixture consisted of the pollutant solution, a known amount of CuO@g-C_3N_4 catalyst, and $NaBH_4$ (98 %, Sigma-Aldrich) as the reducing agent [52,53]. The progress of the reaction was monitored at characteristic wavelengths (λ = 464 nm for MO and λ = 245 nm for ACT) using a UV–Vis spectrophotometer. To optimize reaction parameters, experiments were conducted with varying $NaBH_4$ volumes (0.25, 0.5, 1.0, 1.5 mL; 1×10^{-2} M) and catalyst doses (10, 15, 20, 25 mg), keeping all other conditions constant. The kinetic data were fitted to a pseudo-first-order model to determine rate constants.

2.4. Plasmonic sensing of Cd^{2+} ions

The plasmonic sensing performance of CuO@g-C_3N_4 was evaluated against a range of metal ions (Al^{3+}, Co^{2+}, Fe^{2+}, Na^+, K^+, NO_3^-, Pb^{2+}, OH^-, Cr^{3+}, and Cd^{2+}). For this purpose, chloride salts were employed for cationic species, while potassium nitrate (KNO_3) and potassium hydroxide (KOH) were used as sources of NO_3^- and OH^- anions, respectively. Equal volumes (1:1, *v*/v) of 1 mM metal ion solutions and CuO@g-C_3N_4 aqueous dispersion were mixed, and the UV–Vis spectra were recorded after 20 min. Selectivity experiments revealed a distinct surface plasmon resonance (SPR) red shift exclusively for Cd^{2+}. The effect of varying CuO@g-C_3N_4:Cd^{2+} ratios was then investigated, followed by detection tests in the concentration range of 200–800 μM after 1 h incubation. The limit of detection (LOD) and limit of quantification (LOQ) were calculated according to standard analytical protocols, ensuring reliability and reproducibility of the sensing data.

3. Results and discussion

3.1. Characteristics of CuO@g-C_3N_4 hybrid nanocatalyst

The XRD patterns of the CuO@g-C_3N_4 heterogeneous catalyst are presented in Fig. S1(a). The diffraction peaks of the hybrid material closely match those of standard g-C_3N_4, with additional peaks corresponding to CuO, confirming the successful synthesis of the composite [54]. Compared to pristine g-C_3N_4, the diffraction peaks of CuO@g-C_3N_4 are slightly shifted toward lower 2θ values, which can be attributed to the presence of CuO according to Bragg's law [55,56]. Notably, the reduced full width at half maximum (FWHM) of the crystal planes indicates an increase in crystallite size within the hybrid structure. Furthermore, the absence of any extraneous diffraction peaks beyond those of g-C_3N_4 and CuO demonstrates the high phase purity of the synthesized material. The successful integration of CuO onto the g-C_3N_4 framework was confirmed by XRD analysis, where the diffraction peaks corresponding to monoclinic CuO appeared alongside the characteristic peaks of g-C_3N_4, indicating the formation of a crystalline heterostructure without altering the basic heptazine framework.

The FT-IR spectra of g-C_3N_4 and CuO@g-C_3N_4 are shown in Fig. S1(b). For pristine g-C_3N_4, the broad band observed between 3500 and 3100 cm^{-1} is attributed to N—H stretching vibrations [57,58]. The peaks in the range of 1700–1250 cm^{-1} correspond to CN heterocycle vibrations [59], while the distinct peak at 806 cm^{-1} is assigned to the characteristic *s*-triazine ring vibration [57,60]. The peak at 1230 cm^{-1} is associated with epoxy group vibrations of graphitic carbon. The similarity of the main IR features before and after CuO loading indicates that the g-C_3N_4 framework remains intact following modification. The appearance of a new absorption band at 585 cm^{-1} confirms the presence of Cu—O bonds, evidencing the successful incorporation of CuO nanoparticles [61].

The UV–Vis profiles of g-C_3N_4 and CuO@g-C_3N_4 are presented in Fig. S2(a). Pristine g-C_3N_4 exhibits an absorption edge at ~465 nm, whereas CuO@g-C_3N_4 shows enhanced absorption intensity and a bathochromic shift to ~495 nm, attributable to the CuO modification [62]. Using the Kubelka–Munk function (Fig. S2(b)), the optical band gap of g-C_3N_4 was calculated to be 2.55 eV, higher than that of CuO@g-C_3N_4 (1.84 eV). The red-shifted absorption and narrowed band gap suggest improved visible-light harvesting and potentially enhanced photocatalytic performance for the hybrid material [63]. These changes indicate that CuO modification facilitates potentially enhances electron mobility within the hybrid structure, which can contribute to improved catalytic performance.

The surface morphologies of g-C_3N_4 and CuO@g-C_3N_4 were examined via SEM (Fig. S3(a) and 3(b), respectively). Both materials exhibit two-dimensional lamellar structures; however, the incorporation of CuO results in a transition from larger curled layers (g-C_3N_4) to a mixture of flakes and thin sheets, indicating increased surface area [64]. The CuO modification also leads to smoother surface features and widened lamellar spacing, which is consistent with the slight decrease in crystallinity observed in the XRD results. EDS analysis (Fig. S3(c)) of CuO@g-C_3N_4 prepared at a CuO:g-C_3N_4 mass ratio of 50:1 confirmed the expected elemental weight percentages, while elemental mapping (Fig. S3(d)) revealed a uniform distribution of Cu and O across the g-C_3N_4 surface [65]. In the HRTEM images of CuO@g-C_3N_4 shown in Fig. S4(a), the CuO nanoparticles (NPs) are observed to form spherical-shaped clusters. The corresponding SAED pattern (Fig. S4(b)) further confirms the highly crystalline nature of the CuO NPs, as evidenced by the well-defined diffraction rings arising from the scattering of fine particles. In addition, the SAED pattern reveals the presence of a distinct g-C_3N_4 layer, indicating that the carbon nitride support is well preserved. The TEM images also demonstrate that the CuO NPs are finely dispersed within the nanosheet-like g-C_3N_4 framework, forming a cloud-like distribution that highlights the successful integration of CuO into the g-C_3N_4 matrix (Fig. S4(a)). Such intimate contact between CuO and g-C_3N_4 is expected to facilitate efficient interfacial interactions, which are beneficial for charge separation in photocatalytic processes.

Combined FT-IR, UV–Vis DRS, SEM-EDS and TEM results verify the successful synthesis of the CuO@g-C_3N_4 hybrid catalyst, demonstrating that CuO nanoparticles were uniformly dispersed on the g-C_3N_4 sheets without introducing detectable impurities.

3.2. Degradation of MO and ACT

The catalytic performance of CuO@g-C_3N_4 was evaluated through the reduction of methyl orange (MO) and acetamiprid (ACT), representing typical organic pollutants, in the presence of $NaBH_4$. Fig. 1(a) illustrates the degradation efficiencies and corresponding reaction times under three different experimental conditions: (i) $NaBH_4$ alone, (ii) CuO@g-C_3N_4 alone, and (iii) a combination of CuO@g-C_3N_4 with $NaBH_4$. During the degradation process, a gradual decolorization of the reaction mixture was observed, indicating effective reduction of both dye and pesticide molecules.When $NaBH_4$ (1×10^{-2} M, 1.0 mL) was employed

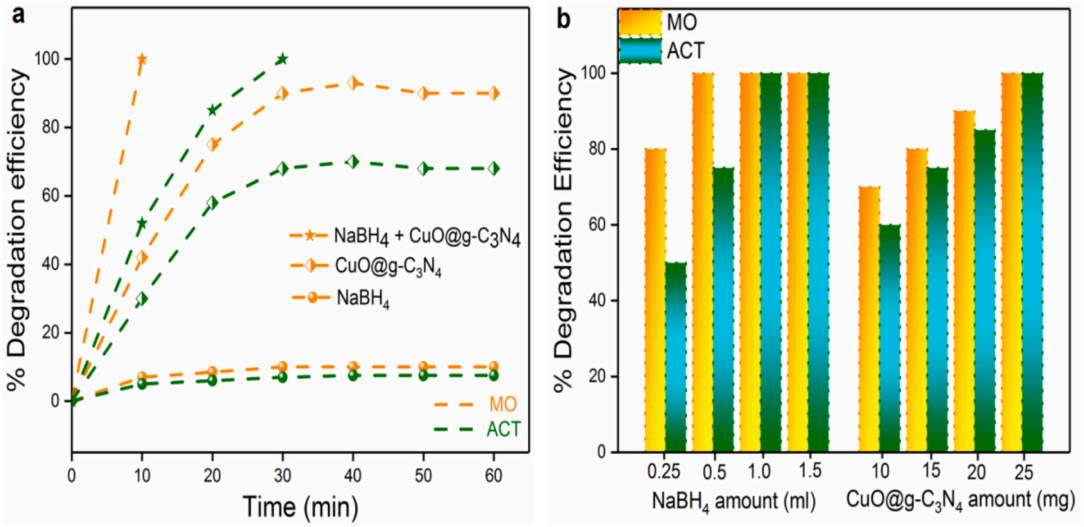

Fig. 1. (a) MO and ACT degradation removal in the presence of only NaBH4, only CuO@g-C_3N_4 and both, and (b) effect graphs of the amount of $NaBH_4$ and CuO@g-C_3N_4 on catalysis efficiency.

without the hybrid catalyst, only ~10 % reduction was achieved even after more than 1 h, highlighting the limited reducing capability of $NaBH_4$ alone. In contrast, the CuO@g-C_3N_4 catalyst (20 mg) without $NaBH_4$ accomplished over 50 % reduction of the pollutants within 20 min, demonstrating its significant adsorption capability. The highest catalytic efficiency was observed when both $NaBH_4$ and CuO@g-C_3N_4 were present. At an initial pollutant concentration of 20 mg/L, complete degradation of MO and ACT was achieved within 8 and 22 min, respectively. These findings confirm the superior performance of CuO@g-C_3N_4 as a heterogeneous catalyst, exceeding the efficiencies reported for similar catalytic systems (Table 1).

The influence of catalyst dosage and $NaBH_4$ concentration on the degradation process was further investigated, as described in Section 2.3, and the results are summarized in Fig. 1(b). An increase in the amount of CuO@g-C_3N_4 led to higher degradation efficiencies for both MO and ACT. This enhancement can be attributed to the greater availability of active sites for electron transfer and adsorption, facilitating more efficient pollutant decomposition [25,53]. Similarly, raising the $NaBH_4$ concentration improved the degradation rates, up to a threshold beyond which no further enhancement was observed—specifically, 0.5 mL for MO and 1.0 mL for ACT. Beyond these concentrations, the excess $NaBH_4$ did not contribute to increased degradation due to the fixed catalyst amount. The observed behavior can be explained by the mechanism in which reactive hydrogens and electrons supplied by $NaBH_4$ are transferred to the pollutant molecules via the catalytic action of CuO@g-C_3N_4, accelerating their reduction [25,53]. Based on these observations, the optimum conditions for the catalytic reduction were established as 20 mg of CuO@g-C_3N_4 with 0.5 mL and 1.0 mL of $NaBH_4$ for MO and ACT, respectively. Under these optimized parameters, the hybrid catalyst demonstrated rapid, efficient, and reproducible removal of the target pollutants, confirming its potential for practical applications in wastewater treatment.

The kinetics of MO and ACT removal over the CuO@g-C_3N_4 hybrid catalyst were analyzed using a pseudo-first-order kinetic model, based on the experimental concentration–time data. The plot of $\ln(C/C_0)$ versus time is presented in Fig. 2, from which the rate constants (k) were determined through linear regression and are summarized in Table 1. The higher rate constant observed for MO degradation indicates that the CuO@g-C_3N_4 catalyst facilitates more efficient reduction of the dye compared to ACT, reflecting its enhanced catalytic activity toward MO under the studied conditions. The λ_max absorption band of MO at 464 nm is attributed to the extended π-conjugated system across the azo linkage, further stabilized by the electron-donating effect of the dimethylamino substituent. A secondary absorption band around 280 nm corresponds to $\pi \rightarrow \pi^*$ electronic transitions within the aromatic system. In contrast, the reduction of MO produces sodium p-aminobenzenesulfonate, which exhibits a distinct absorption peak at 246 nm, the intensity of which progressively increases during the reaction, confirming the gradual formation and accumulation of the reduction product (Fig. 2).

A proposed catalytic reduction mechanism is illustrated in Scheme 2. The copper active sites in CuO@g-C_3N_4 facilitate the transfer of hydride species generated from $NaBH_4$ to the pollutant molecules, thereby accelerating hydrogen evolution and electron transfer. In the case of MO, the azo bond (–N=N–) undergoes symmetrical cleavage, yielding sodium p-aminobenzenesulfonate and *N*,*N*-dimethyl-*p*-phenylenediamine as primary products. Similarly, the reduction of ACT is proposed to produce 2-chloro-5-hydroxymethylpyridine and *N*-cyanomethylamine. The proposed mechanism highlights the dual role of CuO@g-C_3N_4 as both an adsorbent and a catalytic mediator, promoting efficient electron transfer and facilitating rapid degradation of both dye and pesticide molecules.

Table 1
Calculated *k* and %removal of catalytic degradation of pollutants by catalyst.

Pollutants	Catalysist	k (min^{-1})	% Removal	Reference
MO	CuO@g-C_3N_4	0.15 ± 0.001	100	This work
ACT		0.085 ± 0.002	100	
MO	CuO/g-C_3N_4	0.7836	99.7	[49]
4-NP		2.0482	99.5	
RhB	g-C_3N_4/ZrO_2	0.0783	78.61	[66]
MB		0.0921	81.35	
Cr(VI)	g-C_3N_4/Ni_3S_2	0.0255	78	[67]
4-NP	g-C_3N_4/CeO_2	1.8121	86.5	[68]

3.3. Detection of Cd (II) ions

Transition metal oxides such as CuO and graphene derivatives like g-C_3N_4 have attracted significant attention in biosensor applications due to their unique electronic, optical, and surface properties [69]. In the present study, the CuO@g-C_3N_4 hybrid material was investigated for its potential as a plasmonic sensor for Cd^{2+} detection. Monitoring Cd^{2+} is critical because this ion, widely employed in batteries, electronics, pigments, plastics, and coatings, poses severe health risks including respiratory diseases, osteoporosis, kidney damage, and cancer [70,71]. Ten different cation and anion species were tested to assess the

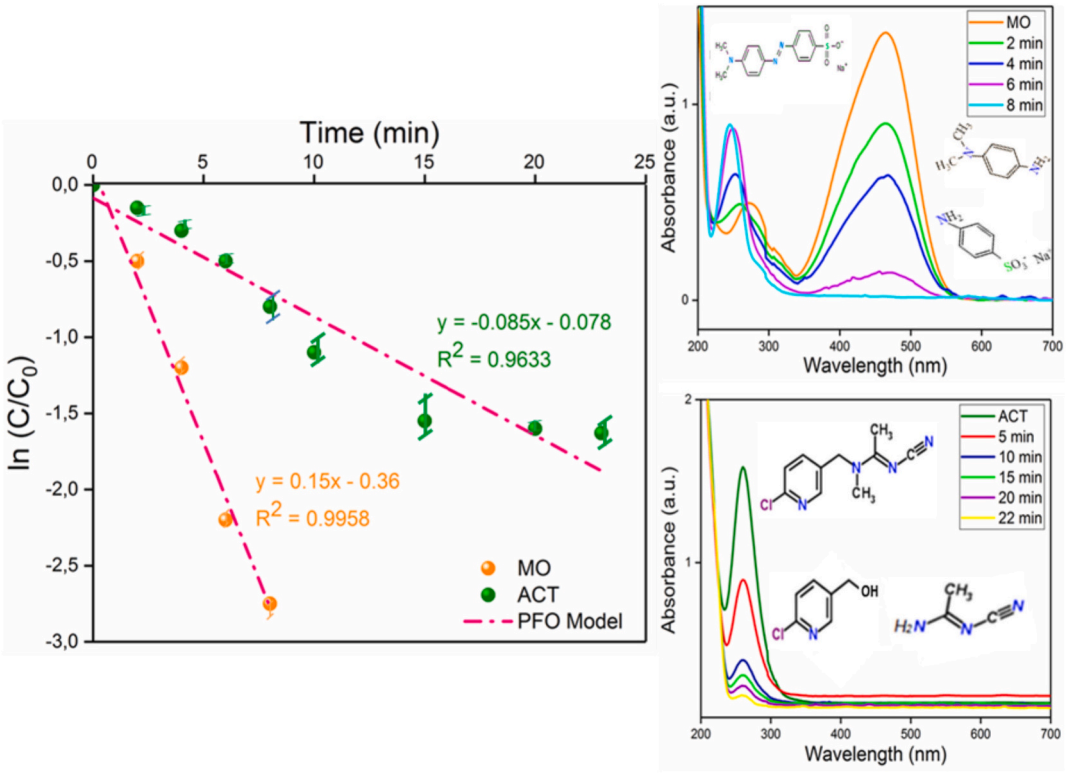

Fig. 2. Pseudo-first-order kinetic models and UV–Visible spectra of catalytic degradation of MO and ACT (inset: molecular structures and degradation products) (Concentration of MO and ACT; 1 mL, 20 mg/L, $NaBH_4$; 1 mL 1 × 10^{-2} mol L^{-1}, CuO@g-C_3N_4 solution with water; 20 mg, 1.5 mL).

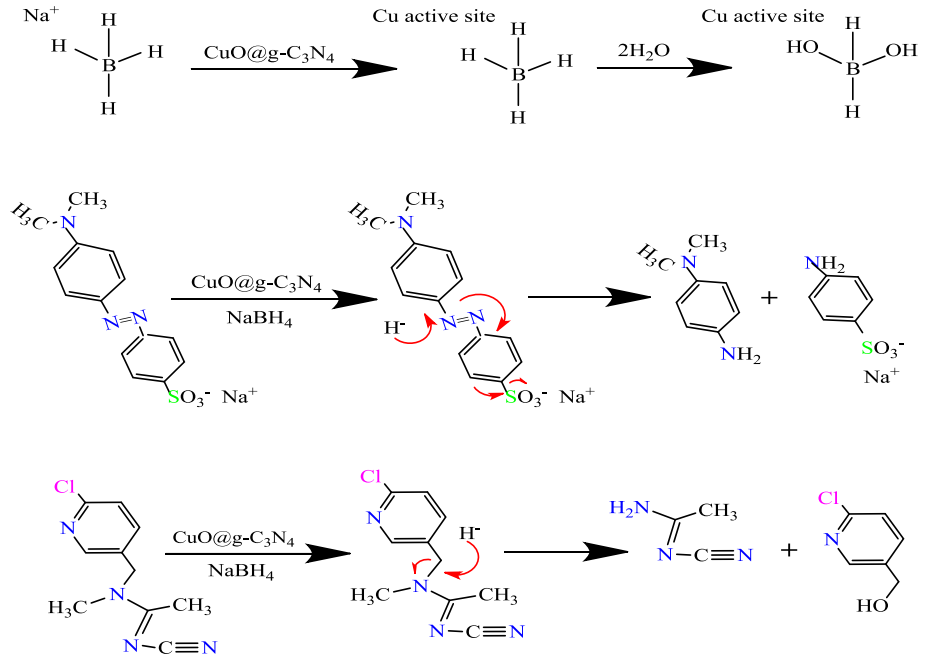

Scheme 2. Proposed degradation mechanism for MO and ACT by using CuO@g-C_3N_4 with $NaBH_4$.

selectivity of the sensor, as described in Section 2.4. Remarkably, only the addition of Cd^{2+} induced a red shift in the surface plasmon resonance (SPR) band of CuO@g-C_3N_4 (Fig. 3(a)), demonstrating high selectivity. SPR-based sensors offer advantages such as rapid response and simultaneous detection, while the distinct SPR features of CuO and g-C_3N_4 enable their synergistic application in plasmonic sensing. The adsorption of Cd^{2+} ions onto the hybrid surface alters the local refractive index, thereby modifying the SPR angle [72,73]. Free electron pairs associated with nitrogen atoms in the g-C_3N_4 framework are believed to facilitate Cd^{2+} binding, while the CuO nanoparticles provide additional active sites for electron transfer and adsorption [72]. To quantitatively evaluate the sensing performance, Cd^{2+} concentrations ranging from 200 μM to 800 μM were examined. A consistent red shift of 20–25 nm in the SPR band was observed with increasing ion concentration (Fig. 3

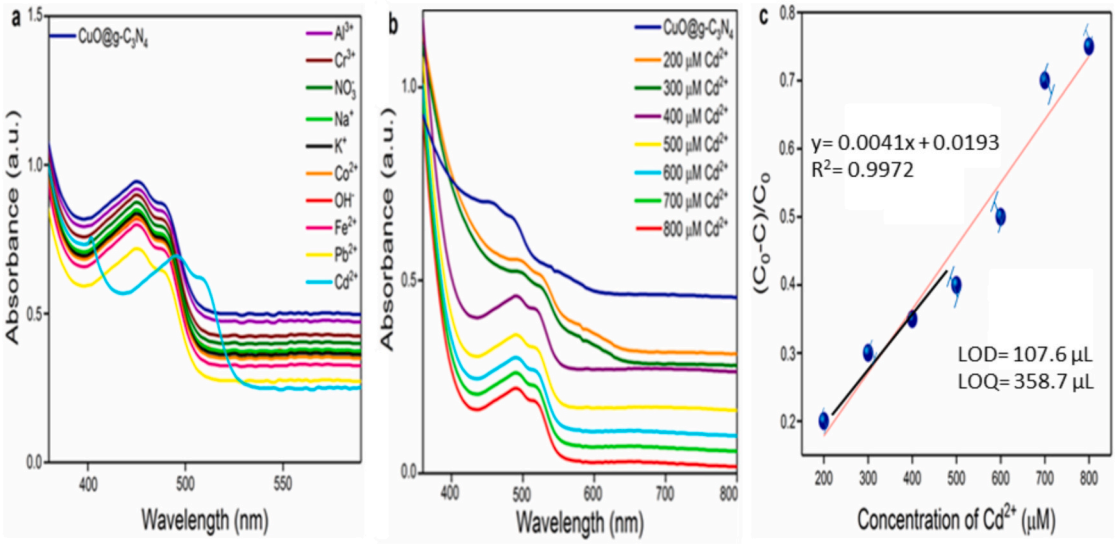

Fig. 3. UV–Vis. spectra of CuO@g-C_3N_4 for different (a) ions and (b) ratios of Cd^{2+}, (c) plot of $(C_0—C)/C_0$ versus different concentrations of Cd^{2+}.

(b)). The corresponding calibration curve (Fig. 3(c)) exhibited a linear response between 200 and 800 μM, with a correlation coefficient of 0.997 [74]. Using a blank solution, the limit of detection (LOD) and limit of quantification (LOQ) were determined to be 107.6 ± 5.1 μM and 358.7 ± 7.3 μM, respectively [75]. Due to the dual adsorption capability of both CuO and g-C_3N_4, a bathochromic shift plateaued above 400 μM, and thus LOD and LOQ values were calculated based on the linear range of 200–400 μM. The strong correlation between structural characterization and sensing performance can be attributed to the uniform dispersion of CuO nanoparticles on the g-C_3N_4 sheets, as confirmed by SEM-EDS, and XRD analyses (Section 3.1). The lamellar morphology of g-C_3N_4 ensures a high surface area for ion adsorption, while CuO sites enhance electron transfer, collectively resulting in effective plasmonic sensing. Consequently, the CuO@g-C_3N_4 hybrid demonstrates not only excellent catalytic reduction capabilities but also sensitive and selective detection of Cd^{2+} ions, highlighting its dual functionality in environmental remediation applications.

4. Conclusions

A novel CuO@g-C_3N_4 hybrid nanosheet was successfully synthesized via a simple two-step process, combining the catalytic properties of g-C_3N_4 with the electronic and surface features of CuO nanoparticles. The resulting nanocomposite exhibited high catalytic efficiency in the $NaBH_4$-assisted reduction of MO and ACT, achieving rapid removal rates governed by pseudo-first-order kinetics under dark conditions. In addition, the material functioned as a selective plasmonic fluorescence sensor for Cd^{2+} ions, showing a clear bathochromic SPR shift and acceptable detection limits. Distinct from previous dual-functional g-C_3N_4 composites that typically couple photocatalysis with sensing, our system uniquely integrates $NaBH_4$-driven catalytic reduction and Cd^{2+} detection on a single CuO@g-C_3N_4 platform. These findings underscore the synergistic benefits of CuO modification in enhancing both reduction and sensing performance, and highlight the promise of this material for practical applications in pollutant remediation and heavy-metal monitoring.

CRediT authorship contribution statement

Muradiye Şahin: Writing – review & editing, Writing – original draft, Visualization, Validation, Methodology, Formal analysis, Data curation, Conceptualization.

Declaration of generative AI and AI-assisted technologies in the writing process

During the preparation of this work the author used ChatGPT in order to only improve language and readability, with caution. After using this tool, the author reviewed and edited the content as needed and take full responsibility for the content of the publication.

Declaration of competing interest

The authors declare that they have no known competing financial interests or personal relationships that could have appeared to influence the work reported in this paper.

Acknowledgment

I would like to express my sincere gratitude to Selçuk University and Kırşehir Ahi Evran University for their laboratory contributions in carrying out this report and to Prof. Dr. İlkay Hilal Gübbük for her support.

Appendix A. Supplementary data

Supplementary data to this article can be found online at https://doi.org/10.1016/j.microc.2025.115600.

Data availability

Data will be made available on request.

References

[1] S. Khettaf, R. Boumaraf, F. Benmahdi, K.-E. Bouhidel, M. Bouhelassa, Removal of the neutral dissolved organic matter (NDOM) from surface water by coagulation/flocculation and nanofiltration, Anal. Lett. 54 (17) (2021) 2713–2726.
[2] A. Pardo, H. Garcia, P. Ramirez, M.A. Carrillo Alvarado, K.S. Krishna, N. Dominguez, M.T. Islam, H. Wang, J.C. Noveron, Self-regenerating photocatalytic hydrogel for the adsorption and decomposition of methylene blue and antibiotics in water, Environ. Technol. Innov. 11 (2018) 321–327.
[3] M. Şahin, Y. Arslan, A. Soyuçok, Helichrysum arenarium-mediated facile green synthesis, antibacterial, catalytic activity and hydrogen evolution of metallic (ag, cu) and bimetallic (ag/cu) nanoparticles, Mater. Chem. Phys. 314 (2024) 128853.
[4] S.A.B. Gilani, F. Naseeb, A. Kiran, M.U. Ihsan, J. Iqbal, H.M.A. Javed, H.N. Bhatti, A.M. Karami, S. Hussain, M. ShabirMahr, pH dependent synthesis of ceria nanoparticles for efficient sunlight-driven photocatalysis of methyl orange containing wastewater, Opt. Mater. 148 (2024) 114871.

[5] E. Serrano, M. Munoz, Z.M. de Pedro, J.A. Casas, Fast oxidation of the neonicotinoid pesticides listed in the EU decision 2018/840 from aqueous solutions, Sep. Purif. Technol. 235 (2020) 116168.
[6] I. Carra, C. Sirtori, L. Ponce-Robles, J.A. Sanchez Perez, S. Malato, A. Agüera, Degradation and monitoring of acetamiprid, thiabendazole and their transformation products in an agro-food industry effluent during solar photo–Fenton treatment in a raceway pond reactor, Chemosphere 130 (2015) 73–81.
[7] L. Zušťíková, D. Bažány, H. Greifová, N. Knížatová, A. Kováčik, N. Lukáč, T. Jambor, Screening of toxic effects of neonicotinoid insecticides with a focus on acetamiprid: a review, Toxics 11 (7) (2023) 598.
[8] M. Dolatabadi, H. Naidu, S. Ahmadzadeh, A green approach to remove acetamiprid insecticide using pistachio shell-based modified activated carbon; economical groundwater treatment, J. Clean. Prod. 316 (2021) 128226.
[9] Y. Wan, T.M. Tran, V.T. Nguyen, A. Wang, J. Wang, K. Kannan, Neonicotinoids, fipronil, chlorpyrifos, carbendazim, chlorotriazines, chlorophenoxy herbicides, bentazon, and selected pesticide transformation products in surface water and drinking water from northern Vietnam, Sci. Total Environ. 750 (2021) 141507.
[10] M. Qiu, Z. Liu, S. Wang, B. Hu, The photocatalytic reduction of U (VI) into U (IV) by ZIF-8/g-C_3N_4 composites at visible light, Environ. Res. 196 (2021) 110349.
[11] D. Pietrzak, J. Kania, E. Kmiecik, G. Malina, K. Wątor, Fate of selected neonicotinoid insecticides in soil–water systems: current state of the art and knowledge gaps, Chemosphere 255 (2020) 126981.
[12] D. Pietrzak, J. Kania, G. Malina, E. Kmiecik, K. Wątor, Pesticides from the EU first and second watch lists in the water environment, Clean-Soil Air Water 47 (7) (2019) 1800376.
[13] A. Cruz-Alcalde, C. Sans, S. Esplugas, Priority pesticides abatement by advanced water technologies: the case of acetamiprid removal by ozonation, Sci. Total Environ. 599-600 (2017) 1454–1461.
[14] M.J. Berens, P.D. Capel, W.A. Arnold, Neonicotinoid insecticides in surface water, groundwater and wastewater across land-use gradients and potential effects, Environ. Toxicol. Chem. 40 (4) (2021) 1017–1033.
[15] M. Yamamuro, T. Komuro, H. Kamiya, T. Kato, H. Hasegawa, Y. Kameda, Neonicotinoids disrupt aquatic food webs and decrease fishery yields, Science 366 (6465) (2019) 620–623.
[16] M. Renaud, T. Akeju, T. Natal-da-Luz, S. Leston, J. Rosa, F. Ramos, J.P. Sousa, H.M. V.S. Azevedo-Pereira, Effects of the neonicotinoids acetamiprid and thiacloprid in their commercial formulations on soil fauna, Chemosphere 194 (2018) 85–93.
[17] E. Sanz-Santos, P. Gutiérrez-Sánchez, Multicomponent and continuous adsorption of neonicotinoid pesticides identified in the EU watch lists onto mesoporous and biogenic activated carbon, Sep. Purif. Technol. 346 (2024) 127514.
[18] F. Deng, E. Brillas, Advances in the decontamination of wastewaters with synthetic organic dyes by electrochemical Fenton-based processes, Sep. Purif. Technol. 316 (2023) 123764.
[19] J.J. Samraj, R. Manju, M.S. Ananthakrishna Tantry, K. Santhakumar, B. Neppolian, New insights into continuous flow reactor systems for the effective degradation of persistent pharmaceutical pollutants using advanced oxidation processes, Chem. Eng. J. 514 (2025) 162585.
[20] J.J. Samraj, R. Manju, M. Ashokkumar, B. Neppolian, Leveraging the critical role of $CoFe_2O_4/ZnWO_4$ heterostructure for the enhanced sonophotocatalytic degradation of tetracycline, chlortetracycline, and chloramphenicol: mechanism insights and pathways, J. Clean. Prod. 492 (2025) 144846.
[21] H. Kumari, R. Suman Sonia, S. Ranga, S. Chahal, S. Devi, S. Sharma, P. Kumar, S. Kumar, A. Kumar, R. Parmar Kumar, A review on photocatalysis used for wastewater treatment: dye degradation, Water Air Soil Pollut. 234 (2023) 349.
[22] M.M. Hassan, H. Li, W. Ahmad, M. Zareef, J. Wang, S. Xie, P. Wang, Q. Ouyang, S. Wang, Q. Chen, Au@Ag nanostructure based SERS substrate for simultaneous determination of pesticides residue in tea via solid phase extraction coupled multivariate calibration, LWT 105 (2019) 290–297.
[23] C. Li, Y. Zhang, W. Cai, X. Zhang, Y. Xie, Y. Guo, H. Yu, W. Yao, H. Qian, Mechanism insights into the transformation of carbosulfan during apple drying processes, Ecotoxicol. Environ. Saf. 201 (2020) 110729.
[24] M.I. Maldonado, S. Malato, L.A. Pérez-Estrada, W. Gernjak, I. Oller, X. Doménech, J. Peral, Partial degradation of five pesticides and an industrial pollutant by ozonation in a pilot-plant scale reactor, J. Hazard. Mater. 138 (2) (2006) 363–369.
[25] M. Şahin, Y. Arslan, F. Tomul, Adsorption, oxidation, kinetic and thermodynamic studies of methyl orange by magnetic Fe_3O_4 NPs and their chitosan/alginate nanocomposites, Int. J. Environ. Anal. Chem. 104 (18) (2024) 6254–6273.
[26] M. Sakr, M.S. Adly, M. Gar Alalm, H. Mahanna, Effective removal of acetamiprid and eosin Y by adsorption on pristine and modified MIL-101 (Fe), Environ. Sci. Pollut. Res. 31 (2024) 41221–41245.
[27] S. Farooq, H. Wu, J. Nie, S. Ahmad, I. Muhammad, M. Zeeshan, R. Khan, M. Asim, Application, advancement and green aspects of magnetic molecularly imprinted polymers in pesticide residue detection, Sci. Total Environ. 804 (2022) 150293.
[28] Z. Fallah, E.N. Zare, M. Ghomi, F. Ahmadijokani, M. Amini, M. Tajbakhsh, M. Arjmand, G. Sharma, H. Ali, A. Ahmad, P. Makvandi, E. Lichtfouse, M. Sillanpää, R.S. Varma, Toxicity and remediation of pharmaceuticals and pesticides using metal oxides and carbon nanomaterials, Chemosphere 275 (2021) 130055.
[29] L. Lian, B. Jiang, Y. Xing, N. Zhang, Identification of photodegradation product of organophosphorus pesticides and elucidation of transformation mechanism under simulated sunlight irradiation, Ecotoxicol. Environ. Saf. 224 (2021) 112655.
[30] P.N. Nelson, A density functional theoretical study of the hydrolysis mechanism of three neonicotinoid based pesticides, J. Mol. Struct. 1230 (2021) 129909.
[31] R. Boumaraf, S. Khettaf, F. Benmahdi, R. Masmoudi, A. Ferhati, Removal of 2, 4-dichlorophenoxyacetic acid from aqueous solutions by nanofiltration and activated carbon, Biomass Convers. Biorefinery 14 (2024) 15689–15704.
[32] M.Q. Seah, Z.C. Ng, G.S. Lai, W.J. Lau, M.A. Al-Ghouti, N.H. Alias, A.F. Ismail, Removal of multiple pesticides from water by different types of membranes, Chemosphere 356 (2024) 141960.
[33] P.S. Goh, N.A. Ahmad, T.W. Wong, L.T. Yogarathinam, A.F. Ismail, Membrane technology for pesticide removal from aquatic environment: status quo and way forward, Chemosphere 307 (3) (2022) 136018.
[34] A.S. Jatoi, Z. Hashmi, R. Adriyani, A. Yuniarto, S.A. Mazari, F. Akhter, N. M. Mubarak, Recent trends and future challenges of pesticide removal techniques–a comprehensive review, J. Environ. Chem. Eng. 9 (4) (2021) 105571.
[35] J. Liu, Z. Wang, Q. Wang, K. Zhang, Y. Luo, Y. Liu, Y. Lyu, B. Huang, Porphyrin-based covalent triazine framework and its carbonized derivative as catalyst scaffold of au and ag nanoparticles for 4-nitrophenol reduction, Microporous Mesoporous Mater. 330 (2022) 111611.
[36] G. Crini, E. Lichtfouse, Advantages and disadvantages of techniques used for wastewater treatment, Environ. Chem. Lett. 17 (2019) 145–155.
[37] P. Hao, Z. Chen, Y. Yan, W. Shi, F. Guo, Recent advances, application and prospect in g-C_3N_4-based S-scheme heterojunction photocatalysts, Sep. Purif. Technol. 330 (2024) 125302.
[38] P.P. Singh, V. Srivastava, Recent advances in visible-light graphitic carbon nitride (g-C_3N_4) photocatalysts for chemical transformations, RSC Adv. 12 (28) (2022) 18245–18265.
[39] L. Acharya, B.P. Mishra, S.P. Pattnaik, R. Acharya, K. Parida, Incorporating nitrogen vacancies in exfoliated B-doped g-C_3N_4 towards improved photocatalytic ciprofloxacin degradation and hydrogen evolution, New J. Chem. 46 (7) (2022) 3493–3503.
[40] M. Wu, J.M. Yan, X. Zhang, M. Zhao, Synthesis of g-C_3N_4 with heating acetic acid treated melamine and its photocatalytic activity for hydrogen evolution, Appl. Surf. Sci. 354 (2015) 196–200.
[41] C. Zhang, Y. Li, D. Shuai, W. Zhang, L. Niu, L. Wang, H. Zhang, Visible-light-driven, water-surface-floating antimicrobials developed from graphitic carbon nitride and expanded perlite for water disinfection, Chemosphere 208 (2018) 84–92.
[42] Z. Asghar, H. Habib, J.A. Jrar, F.K. Alauddin, K. Butt, Y. Zheng, J. Zhang, X. Wang Hou, Engineering Schottky barrier and enhancing charge transfer kinetics via red phosphorus nanoparticles on g-C_3N_4/Ti_3C_2 for superior photocatalytic H_2 production and CO_2 reduction, Int. J. Hydrog. Energy 155 (2025) 150182.
[43] Z. Asghar, H. Habib, M. Bilal, Z.U. Rehman, F.K. Butt, K. Zheng, Y. Liu, H. Lin, Y. Zhang, X. Wang, J. Hou, Enhancing electron-hole pair generation by Ti_3C_2 MXene-derived TiO_2 integrated with g-C_3N_4 heterojunction for excellent photocatalytic H_2 production and CO_2 reduction, Int. J. Hydrog. Energy 149 (2025) 150052.
[44] A. Mishra, A. Mehta, S. Basu, N.P. Shetti, K.R. Reddy, T.M. Aminabhavi, Graphitic carbon nitride (g–C_3N_4)–based metal-free photocatalysts for water splitting: a review, Carbon 149 (2019) 693–721.
[45] A. Raza, H. Shen, A.A. Haidry, S. Cui, Hydrothermal synthesis of Fe_3O_4/TiO_2 /g-C_3N_4: advanced photocatalytic application, Appl. Surf. Sci. 488 (2019) 887–895.
[46] Y.M. Dai, W.J. Chen, C.M. Chang, Construction of heterostructured nanorods-like ZnO/g-C_3N_4 nanocomposite to obtain enhanced photocatalytic properties, Opt. Mater. 148 (2024) 114925.
[47] N.A. Chopan, H.T.N. Chishti, Polypyrrole-decorated ZnO/g-C_3N_4 S-scheme photocatalyst for rhodamine B dye degradation: mechanism and antibacterial activity, Mater. Today Chem. 32 (2023) 101643.
[48] U.K. Ghorui, P. Mondal, J. Satra, B. Adhikary, A. Mondal, *In situ* metallic copper incorporation into novel g-$C_3N_4/ZnWO_4$ nanocomposite semiconductor for efficient thin film solar cell application, Mater. Sci. Semicond. Process. 143 (2022) 106559.
[49] R. Suresh, N.S. Karthikeyan, L. Gnanasekaran, S. Rajendran, M. Soto-Moscoso, Facile synthesis of CuO/g-C_3N_4 nanolayer composites with superior catalytic reductive degradation behavior, Chemosphere 315 (2023) 137711.
[50] S. Ganesan, T. Kokulnathan, S. Sumathi, A. Palaniappan, Efficient photocatalytic degradation of textile dye pollutants using thermally exfoliated graphitic carbon nitride (TE–g–C_3N_4), Sci. Rep. 14 (2024) 2284.
[51] K. Atacan, M. Özacar, Construction of a non-enzymatic electrochemical sensor based on CuO/g-C_3N_4 composite for selective detection of hydrogen peroxide, Mater. Chem. Phys. 266 (2021) 124527.
[52] M. Şahin, İ.H. Gübbük, Green synthesis of palladium nanoparticles and investigation of their catalytic activity for methylene blue, methyl orange and rhodamine B degradation by sodium borohydride, React. Kinet. Mech. Catal. 135 (2022) 999–1010.
[53] M. Şahin, Y. Arslan, F. Tomul, B. Yıldırım, H. Genç, Green synthesis of silver nanoparticles using Lathyrus brachypterus extract for efficient catalytic reduction of methylene blue, methyl orange, methyl red and investigation of a kinetic model, React. Kinet. Mech. Catal. 135 (2022) 3303–3315.
[54] X. Liu, S. Cui, Z. Sun, Y. Ren, X. Zhang, P. Du, Self-supported copper oxide electrocatalyst for water oxidation at low overpotential and confirmation of its robustness by cu K-edge X-ray absorption spectroscopy, J. Phys. Chem. C 120 (2016) 831–840.
[55] M.W. Kadi, R.M. Mohamed, A.A. Ismail, D.W. Bahnemann, Soft and hard templates assisted synthesis mesoporous CuO/g-C_3N_4 heterostructures for highly enhanced and accelerated Hg(II) photoreduction under visible light, J. Colloid Interface Sci. 580 (2020) 223–233.
[56] C.G. Pope, X-ray diffraction and the bragg equation, J. Chem. Educ. 74 (1997) 129–131.

[57] J. Yan, X. Han, X. Zheng, J. Qian, J. Liu, X. Dong, F. Xi, One-step template/chemical blowing route to synthesize flake-like porous carbon nitride photocatalyst, Mater. Res. Bull. 94 (2017) 423–427.
[58] L. Zhou, H. Zhang, H. Sun, S. Liu, M.O. Tade, S. Wang, W. Jin, Recent advances in non-metal modification of graphitic carbon nitride for photocatalysis: a historic review, Catal, Sci. Technol. 6 (2016) 7002–7023.
[59] A. Ben-Refael, I. Benisti, Y. Paz, Transient photoinduced phenomena in graphitic carbon nitride as measured at nanoseconds resolution by step-scan FTIR, Catal. Today 340 (2020) 97–105.
[60] H. Ghafuri, Z. Tajik, N. Ghanbari, P. Hanifehnejad, Preparation and characterization of graphitic carbon nitride-supported l-arginine as a highly efficient and recyclable catalyst for the one-pot synthesis of condensation reactions, Sci. Rep. 11 (2021) 19792.
[61] H. Veisi, B. Karmakar, T. Tamoradi, S. Hemmati, M. Hekmati, M. Hamelian, Biosynthesis of CuO nanoparticles using aqueous extract of herbal tea (Stachys Lavandulifolia) flowers and evaluation of its catalytic activity, Sci. Rep. 11 (2021) 1983.
[62] S. Sarkar, S.S. Sumukh, K. Roy, N. Kamboj, T. Purkait, M. Das, R.S. Dey, Facile one step synthesis of cu-g-C_3N_4 electrocatalyst realized oxygen reduction reaction with excellent methanol crossover impact and durability, J. Colloid Interface Sci. 558 (2020) 182–189.
[63] T.P. Vijayakumar, M.D. Benoy, J. Duraimurugan, G. Suresh Kumar, M. Shkir, P. Maadeswaran, A. Senthil Kumar, K.A. Ramesh Kumar, Hydrothermal synthesis of CuO/g-C_3N_4 nanosheets for visible-light driven photodegradation of methylene blue, Diam. Relat. Mater. 121 (2022) 108735.
[64] M.A. Bajiri, A. Hezam, K. Namratha, R. Viswanath, Q.A. Drmosh, H.S. Bhojya Naik, K. Byrappa, CuO/ZnO/g-C_3N_4 heterostructures as efficient visible light-driven photocatalysts, J. Environ. Chem. Eng. 7 (5) (2019) 103412.
[65] C. Qin, Y. Wang, Y. Gong, Z. Zhang, J. Cao, CuO-ZnO hetero-junctions decorated graphitic carbon nitride hybrid nanocomposite: hydrothermal synthesis and ethanol gas sensing application, J. Alloys Compd. 770 (2019) 972–980.
[66] D. Venkatesh, G. Deepthi, K. Girija Mangatayaru, M. Noorjahan, Hydrothermal synthesis of g-C_3N_4/ZrO_2 nanocomposites for the photocatalytic degradation of dyes and selective sensing of heavy metal ions, Mater Today Proc 92 (2) (2023) 1344–1351.
[67] B. Niu, X. Li, D. Lin, X. Chen, Z. Chen, H. Guo, Highly efficient noble metal-free g-C_3N_4@ Ni_xS_y nanocomposites for catalytic reduction of nitrophenol, azo dyes and Cr(VI), Inorg. Chem. Commun. 142 (2022) 109589.
[68] D. Venkatesh, G. Deepthi, K. Girija Mangatayaru, M. Noorjahan, Ultrasound-assisted synthesis, spectral and analytical analysis of g-C_3N_4/CeO_2 composites towards catalytic reduction of nitroaromatic compounds & selective fluorescence detection of Hg^{2+}, Results Chem. 4 (2022) 100598.
[69] H. Hu, A. Zavabeti, H. Quan, W. Zhu, H. Wei, D. Chen, J.Z. Ou, Recent advances in two-dimensional transition metal dichalcogenides for biological sensing, Biosens. Bioelectron. 142 (2019) 111573.
[70] M. Şahin, M. Atasoy, Y. Arslan, D. Yildiz, Removal of Ni (II), cu (II), Pb (II), and cd (II) from aqueous phases by silver nanoparticles and magnetic nanoparticles/nanocomposites, ACS Omega 8 (2023) 34834–34843.
[71] M. Şahin, Y. Arslan, M. Atasoy, M. Sillanpää, Adsorption performance of Zn(II)-based coordination polymer (ZnMOF) reinforced magnetic activated biochar (CmBC-Fe_3O_4@ZnMOF) hybrid composites, Water Environ. Res. 97 (6) (2025) 70113.
[72] C. Boozer, G. Kim, S. Cong, H.W. Guan, T. Londergan, Looking towards label-free biomolecular interaction analysis in a high-throughput format: a review of new surface plasmon resonance technologies, Curr. Opin. Biotechnol. 17 (2006) 400–405.
[73] A. Kumar, A.K. Yadav, A.S. Kushwaha, S.K. Srivastava, A comparative study among WS_2, MoS_2 and graphene based surface plasmon resonance (SPR) sensor, Sens. Actuator. Rep. 2 (1) (2020) 100015.
[74] T.H.A. Nguyen, V.-C. Nguyen, T.N.H. Phan, V.T. Le, Y. Vasseghian, M.A. Trubitsyn, A.-T. Nguyen, T.P. Chau, V.-D. Doan, Novel biogenic silver and gold nanoparticles for multifunctional applications: green synthesis, catalytic and antibacterial activity, and colorimetric detection of Fe(III) ions, Chemosphere 287 (2022) 132771.
[75] T. Dang-Bao, T.-S. Nguyen, N.-T. Tran-Dinh, H.-H. Lam, H.-P. Phan, Taking advance of isotropic-to-anisotropic morin-modified silver nanoparticles for simultaneous colorimetric sensing of trivalent chromium and iron ions, Chem. Phys. Imp. 6 (2023) 100245.